Contents lists available at ScienceDirect

Engineering Analysis with Boundary Elements

journal homepage: www.elsevier.com/locate/enganabound

A direct meshless local collocation method for solving stochastic Cahn–Hilliard–Cook and stochastic Swift–Hohenberg equations

Mostafa Abbaszadeh [c], Amirreza Khodadadian [b,*], Maryam Parvizi [b], Mehdi Dehghan [c], Clemens Heitzinger [a,b]

[a] School of Mathematical and Statistical Sciences, Arizona State University, Tempe, AZ 85287, USA
[b] Institute for Analysis and Scientific Computing, Vienna University of Technology (TU Wien), Wiedner Hauptstraße 8–10, Vienna 1040, Austria
[c] Department of Applied Mathematics, Faculty of Mathematics and Computer Sciences, Amirkabir University of Technology, No. 424, Hafez Ave., Tehran 15914, Iran

ARTICLE INFO

ABSTRACT

In this study, the direct meshless local Petrov–Galerkin (DMLPG) method has been employed to solve the stochastic Cahn–Hilliard–Cook and Swift–Hohenberg equations. First of all, we discretize the temporal direction by a finite difference scheme. In order to obtain a fully discrete scheme the direct meshless local collocation method is used to discretize the spatial variable and the Euler–Maruyama method is used for time discretization. The used method is a truly meshless technique. In order to illustrate the efficiency and accuracy of the explained numerical technique, we study two stochastic models with their applications in biology and engineering, i.e., the stochastic Cahn–Hilliard–Cook equation and a stochastic Swift–Hohenberg model.

1. Introduction

The Cahn–Hilliard equation is a robust mathematical model for describing phase separation phenomena in different engineering fields such as copolymer systems and lipid membranes. The equation is used to model binary metal alloys [1], polymers [2] as well as cell proliferation and adhesion [3]. In material science, when a binary alloy is sufficiently cooled down, we observe a partial nucleation or spinodal decomposition, i.e., the material quickly becomes inhomogeneous. In other words, after a few seconds, material coarsening will have happened [4]. The spinodal decomposition is modeled by the Cahn–Hilliard model. The Swift–Hohenberg equation is a mathematical model for scalar fields that has been mostly used as a model for the study of various issues in pattern formation including effects of noise on bifurcations, pattern selection, spatiotemporal chaos and the dynamics of defects [5,6].

Both equations are fourth-order nonlinear PDEs in space and first order in time for which an analytical treatment is not possible. For the Cahn–Hilliard equation, there are different numerical methods for solving the equation such as the finite element method (FEM) [7], isogeometric finite element method [8], least squares spectral element method [9], radial basis functions (RBF) [10] and meshless local collocation methods [11]. The finite difference technique is a popular numerical approach to solve Swift–Hohenberg equation [12,13].

Generally, we can classify the meshless approaches into the strong form, the weak form, and the local weak form. The meshless methods based on the strong form use a set of basis functions to approximate the unknown function where this case is based on the collocation method. For the strong form of meshless methods, we can mention the radial basis functions (RBFs), the radial point interpolation method (RPIM) in addition to the moving least squares (MLS) approximation. The second case of meshless methods is based on the weak form. The mentioned case is very similar to the finite element method (FEM) where the main difference is that the test and trial functions are based on the radial functions, e.g., RBFs, MLS, and other radial functions. For this class, we can mention the element-free Galerkin (EFG) technique. The last class is the local weak form method in the sense that the meshless methods based on the local weak form are truly meshless. For example, meshless local Petrov–Galerkin (MLPG) method, meshless local radial point interpolation method (RPIM), direct MLPG (DMLPG), etc.

---

* Corresponding author.
E-mail addresses: m.abbaszadeh@aut.ac.ir (M. Abbaszadeh), amirreza.khodadadian@tuwien.ac.at (A. Khodadadian), maryam.parvizi@tuien.ac.at (M. Parvizi), mdehghan@aut.ac.ir (M. Dehghan), clemens.heitzinger@tuwien.ac.at (C. Heitzinger).

The MLPG method was for the first time introduced by Atluri and the co-workers [14]. This technique is based on the moving least squares (MLS) approximation. A new class of MLS approximation proposed in [15] is the so-called generalized MLS (GMLS) approximation. Also, according to the new shape functions, a new class of MLPG method that is well-known as the direct MLPG (DMLPG) technique presented in [16]. The DMLPG technique has been applied to solve problems such as heat conduction problems [17], time fractional advection–diffusion equation [18], interface problems [19], two- and three-dimensional potential models [20] and 3D Poisson equations [21], the meshless local radial point interpolation technique to solve 3D wave equations [22], meshless local boundary integral equation for boundary values problems [23], a point interpolation meshless method for solid mechanics problems [24], etc. The interested reader can also see [25] for more details on the DMLPG method.

In this paper, a direct meshless local collocation method based on the direct meshless local Petrov–Galerkin (DMLPG) method is introduced for solving stochastic Cahn–Hilliard–Cook and Swift–Hohenberg equations. The equations in the current paper have direct applications in biology. These equations have been solved by powerful techniques such as discontinuous Galerkin and finite volume methods. The main aim of the current paper is to propose a direct local collocation method for solving the stochastic Cahn–Hilliard–Cook and Swift–Hohenberg equations. The presented technique allows for simple and efficient implementation. Furthermore, another advantage of the proposed technique is that the CPU time by the present method is less than other meshless techniques, which is shown in the numerical results.

The rest of the paper is organized as follows. In Section 2, we present briefly two model equations, i.e., a stochastic Cahn–Hilliard–Cook equation and a stochastic Swift–Hohenberg equation. In Section 3, we introduce the generalized moving least square method and explain the space and time discretizations of the equations. Then, in Section 4 we present five specific test problems where in all cases the meshless technique, as well as the Euler–Maruyama method, are used to obtain the solution. Finally, the conclusions are drawn in Section 5.

2. The model equations

2.1. The stochastic Cahn–Hilliard–Cook equation

The Cahn–Hilliard (CH) equation was introduced by Cahn and Hilliard [1,26]. The equation has been widely used to describe phase separation phenomena in material science (binary alloys), biology (lipid membranes) and engineering (polymer solutions and blends). The equation is described as

$$u_t = \nabla \cdot \left(M \nabla \left(-\gamma \Delta u + \Phi'(u) \right) \right) \qquad \text{in } \Omega \times [0, T], \tag{1}$$

with the boundary conditions

$$\frac{\partial u}{\partial \nu} = 0, \quad \frac{\partial \left(-\gamma \Delta u + \Phi'(u) \right)}{\partial \nu} = 0 \quad \text{on } \partial \Omega \times [0, T] \tag{2}$$

and the initial condition

$$u(x, 0) = u_0(x) \quad \forall x \in \Omega, \tag{3}$$

where $\gamma, M \in \mathbb{R}^+$ and Ω is the computational geometry. Furthermore, $\Phi(u)$ is one of the functions

$$\Phi(u) = \frac{1}{4} u^2 (1 - u)^2, \quad \Phi(u) = \frac{1}{4} \left(u^4 - 2u \right)^2, \quad \Phi(u) = \frac{1}{4} \left(1 - u^2 \right)^2. \tag{4}$$

The solution of the equation u is a rescaled density of atoms or concentration of one of the material components where, usually $u \in [-1, 1]$. Also, we can mention grain growth [27], tumor growth [28], modeling of martensitic phase transformation [29], two-layer channel flow [30] as the application of the equation in applied/material science.

The Cahn–Hilliard–Cook equation presents a more realistic model including the internal thermal fluctuations. It can be derived from (1) by adding thermal noise resulting in

$$\frac{du}{dt} = M \Delta \left(\Phi'(u) - \gamma \Delta u \right) + \sigma \xi \qquad \text{in } \Omega \times [0, T], \tag{5a}$$

$$\frac{\partial u}{\partial \nu} = 0, \quad \frac{\partial \Delta u}{\partial \nu} = 0 \qquad \text{on } \partial \Omega \times [0, T], \tag{5b}$$

where ξ indicates the white noise (i.e., the derivative of the Q-Wiener process) and σ is the noise intensify measure. The system enables us to consider the thermal fluctuations directly in the sense of the Cahn–Hilliard–Cook (CHC) equation by a conserved noise source term. The thermal fluctuations have a substantial effect on the early stage of phase dynamics such as initial dynamics of nucleation [31]. In [32], we implemented the multilevel Monte Carlo method to solve the equation. In that paper, the authors used the finite elements for the spatial discretization and the Euler–Maruyama technique for the time direction.

2.2. Stochastic Swift–Hohenberg equation

Swift and Hohenberg introduced the Swift–Hohenberg equation [33] as follows

$$\frac{\partial u}{\partial t} = -\mu(u) - Dk^4 u - 2Dk^2 \Delta u - D\Delta^2 u \quad \text{in } \Omega \times [0, T] \tag{6}$$

with the boundary conditions

$$\frac{\partial u}{\partial \nu} = 0, \quad \frac{\partial \left(2Dk^2 u + D\Delta u \right)}{\partial \nu} = 0 \quad \text{on } \partial \Omega \times [0, T] \tag{7}$$

and the initial condition

$$u(\mathbf{x}, 0) = u_0(\mathbf{x}) \qquad \forall \mathbf{x} \in \Omega, \tag{8}$$

where $k, D \in \mathbb{R}^+$. Model (6) has been recently studied by fully-discrete algorithm [34], B-spline functions [34], homotopy analysis method (HAM) [35], finite difference approach [12], Fourier spectral procedure [36], etc. Also, the interested reared can refer to [37–39] for more details.

The Swift–Hohenberg equation has several applications in engineering such as physics of foams, cellular materials and metallurgy [40]. In addition, the equation is used to capture the main features of the laser dynamics in so-called class A and C lasers [41]. Also, the Swift–Hohenberg model is used efficiently in the pattern formation [42] and Rayleigh–Bénard convection [43].

The stochastic Swift–Hohenberg equation can be written by adding the derivative of the Q-Wiener process to (6) to find

$$\frac{\partial u}{\partial t} = -\mu(u) - Dk^4 u - 2Dk^2 \Delta u - D\Delta^2 u + \sigma \xi \quad \text{in } \Omega \times [0, T], \tag{9}$$

where the same boundary and initial conditions are applied. As an example, the noise models small irregular fluctuations generated by microscopic effects in the flux of molecular collision. Therefore the stochastic equation can be considered to be a more realistic model [44].

3. Generalized moving least squares approximation

Let a discretization of the boundary value problem based on a set of nodes $\mathbf{X} = \left\{ \mathbf{x}_1, \mathbf{x}_2, \ldots, \mathbf{x}_N \right\}$ be

$$\vartheta_k(u) = \beta_k, \quad 1 \leq k \leq M, \tag{10}$$

where $\vartheta_1, \vartheta_2, \ldots, \vartheta_M$ are linear functionals ($M \geq N$) and β_k are constant. The meshless methods are constructed on a suitable approximation $\hat{\vartheta}_k$ of ϑ_k. Thus, we have to

find real coefficient functions $a_j(\vartheta_k)$ such that

$$\vartheta_k(u) \approx \hat{\vartheta}_k(u) = \sum_{j=1}^{M} a_j(\vartheta_k) u(x_j), \quad 1 \le k \le M. \tag{11}$$

Recently, the authors of [15] proposed a generalization of the MLS approach that it is well-known as *GMLS approximation*. The GMLS approximation is based on the approximation of $\vartheta(u)$ by the linear functionals $\{\gamma_j(u)\}_{j=1}^{N}$. Let

$$\vartheta(u) \approx \hat{\vartheta}(u) = \sum_{j=1}^{N} a_j(\vartheta) \gamma_j(u), \tag{12}$$

where the coefficients a_j are linear in ϑ. Assume relation (12) is exact for a finite dimensional subspace of $\mathbf{P}_m^d = \mathrm{span}\{p_1, p_2, \dots, p_Q\}$ where p_i are polynomial functions. Then, we have

$$\sum_{j=1}^{N} a_j(\vartheta) \gamma_j(p) = \vartheta(p) \qquad \forall p \in \mathbf{P}_m^d. \tag{13}$$

The GMLS approximation can be derived by minimizing the weighted discrete of the L_2-norm

$$J(p) := \sum_{j=1}^{N} \left(\gamma_j(u) - \gamma_j(p) \right)^2 W(\vartheta; \gamma_j), \tag{14}$$

and thus finding

$$p^* = \underset{p \in \mathbf{P}_m^d}{\mathrm{argmin}} \, J(p), \tag{15}$$

where $W(\lambda; \gamma_j)$ is a weight function. Since $p \in \mathbf{P}_m^d$ we have

$$p(\mathbf{x}) = \sum_{i=1}^{Q} l_i p_i(\mathbf{x}). \tag{16}$$

Because of property of the linearity of the functional γ_j, (16) is derived as

$$\gamma_j(p(\mathbf{x})) = \sum_{i=1}^{Q} l_i \gamma_j(p_i(\mathbf{x})) = \mathbf{p}_{\gamma_j}^T \mathbf{l}, \tag{17}$$

where

$$\mathbf{p}_{\gamma_j} = \left[\gamma_j(p_1(\mathbf{x}), \gamma_j(p_2(\mathbf{x}), \dots, \gamma_j(p_Q(\mathbf{x}) \right]^T, \quad \mathbf{l} = \left[l_1, l_2, \dots, l_Q \right]^T. \tag{18}$$

Using the above explanations, functional (14) is equal to

$$J(\mathbf{p}) = \sum_{j=1}^{N} \left(\gamma_j(u) - \mathbf{p}_{\gamma_j}^T \mathbf{l} \right)^2 W(\vartheta; \gamma_j). \tag{19}$$

Let

$$\mathbf{Q}^* = (\mathbf{M}(\vartheta; \gamma))^{-1} \mathbf{B}(\vartheta; \gamma) \hat{\boldsymbol{\gamma}}(u), \tag{20}$$

be the solution of problem (19) where

$$\mathbf{M}(\vartheta; \gamma) = \mathbf{P}_\gamma \mathbf{W}(\vartheta; \gamma) \mathbf{P}_\gamma^T, \quad \mathbf{B}(\vartheta; \gamma) = \mathbf{P}_\gamma \mathbf{W}(\vartheta; \gamma), \quad \mathbf{P}_\gamma = \left[p_{\gamma_1}, p_{\gamma_2}, \dots, p_{\gamma_N} \right],$$

$$\mathbf{W}(\vartheta; \gamma) = \mathrm{diag} \left[W(\vartheta; \gamma_1), W(\vartheta; \gamma_2), \dots, W(\vartheta; \gamma_N) \right],$$

$$\hat{\boldsymbol{\gamma}}(u) = \left[\gamma_1(u), \gamma_2(u), \dots, \gamma_N(u) \right]^T.$$

So, the approximation $\hat{\vartheta}(u)$ of $\vartheta(u)$ is

$$\vartheta(u) = \vartheta(p^*) = \mathbf{p}_\vartheta^T \mathbf{Q}^* = \mathbf{p}_\vartheta^T (\mathbf{M}(\vartheta; \gamma))^{-1} \mathbf{B}(\vartheta; \gamma) \hat{\boldsymbol{\gamma}}(u). \tag{21}$$

We use the quartic spline function as the wight function in the GMLS approximation

$$W(\mathbf{x} - \mathbf{x}_i) = \begin{cases} 1 - 6r_i^2 + 8r_i^3 - 3r_i^4, & r_i \le 1, \\ 0, & r_i > 1, \end{cases} \tag{22}$$

such that $r_i = \dfrac{\|x - x_i\|}{r_w}$ is the size of the support of the weight function.

3.1. Spatial discretization process

In order to achieve a full-discrete scheme based on the DMLPG 2, we introduce the notations

$$\vartheta_{1,i}(U^n) := U^n(\mathbf{x}_i) \approx \widetilde{U}^n(\mathbf{x}_i) = \sum_{j=1}^{N_g} a_{1,j}(\mathbf{x}_i) U^n(\mathbf{x}_i),$$

$$\vartheta_{2,i}(U^n) := \Delta U^n(\mathbf{x}_i) \approx \widetilde{\mu}_{2,i}(U^n) = \sum_{j=1}^{N_g} a_{2,j}(\mathbf{x}_i) U^n(\mathbf{x}_i).$$

Also, from the GMLS approximation, we have

$$\mathbf{a}_{k,:}^T(\mathbf{x}_i) = \vartheta_{k,i}(\mathbf{p}^T) \mathbf{M}^{-1} \mathbf{B}, \qquad k = 1, 2, \tag{23}$$

and according to (21), we obtain

$$\vartheta_{1,i}(\mathbf{p}^T) = \left[p_1(\mathbf{x}_i) \quad p_2(\mathbf{x}_i) \quad \dots \quad p_Q(\mathbf{x}_i) \right],$$

$$\vartheta_{2,i}(\mathbf{p}^T) = \left[\Delta p_1(\mathbf{x}_i) \quad \Delta p_2(\mathbf{x}_i) \quad \dots \quad \Delta p_Q(\mathbf{x}_i) \right].$$

Also, the boundary conditions can be applied by GMLS collocation. For example, we consider the equation

$$u_t = \nabla \cdot \left(M \nabla \left(-\gamma \Delta u + \Phi'(u) \right) \right) + \sigma \xi \qquad \text{in } \Omega \times [0, T], \tag{24}$$

with the boundary conditions

$$\frac{\partial u}{\partial \nu} = 0, \qquad \frac{\partial \left(-\gamma \Delta u + \Phi'(u) \right)}{\partial \nu} = 0 \qquad \text{on } \partial\Omega \times [0, T]. \tag{25}$$

By defining the new variable

$$\Psi := -\gamma \Delta u + \Phi'(u), \tag{26}$$

we have

$$\begin{cases} u_t = \nabla \cdot (M\Psi) + \sigma \xi, \\ \Psi = -\gamma \Delta u + \Phi'(u) \end{cases} \tag{27}$$

with the new boundary conditions

$$\frac{\partial u}{\partial \nu} = 0, \qquad \frac{\partial \Psi}{\partial \nu} = 0 \qquad \text{on } \partial\Omega \times [0, T]. \tag{28}$$

Let $u^n = u(\mathbf{x}, \mathbf{t}_n)$ for all $\mathbf{x} \in \Omega$. Now, by using a finite difference scheme, Eq. (27) can be rewritten as

$$\begin{cases} \dfrac{u^n - u^{n-1}}{\tau} = \dfrac{\nabla \cdot \Psi^n + \nabla \cdot \Psi^{n-1}}{2} + \sigma \xi, \\ \Psi^n = -\gamma \Delta u^n + \Phi'(u^n), \end{cases} \tag{29}$$

and then, by simplification, we have

$$\begin{cases} u^n - \dfrac{\tau}{2} \nabla \cdot \Phi^n = u^{n-1} + \dfrac{\tau}{2} \nabla \cdot \Phi^{n-1} + \tau \sigma \xi, \\ \Psi^n = -\gamma \Delta u^n + \Phi'(u^n). \end{cases} \tag{30}$$

Now, we define

$$\vartheta_{1,i}(u^n) := u^n(\mathbf{x}_i) \approx \sum_{j=1}^{N_g} a_{1,j}(\mathbf{x}_i) u^n(\mathbf{x}_i),$$

$$\vartheta_{2,i}(\Psi^n) := \Psi^n(\mathbf{x}_i) \approx \sum_{j=1}^{N_g} a_{2,j}(\mathbf{x}_i) \Psi^n(\mathbf{x}_i),$$

$$\vartheta_{3,i}(u^n) := \Delta u^n(\mathbf{x}_i) \approx \sum_{j=1}^{N_g} a_{3,j}(\mathbf{x}_i) u^n(\mathbf{x}_i),$$

$$\vartheta_{4,i}(\Psi^n) := \nabla \cdot \Psi^n(\mathbf{x}_i) \approx \sum_{j=1}^{N_g} a_{4,j}(\mathbf{x}_i) \Psi^n(\mathbf{x}_i),$$
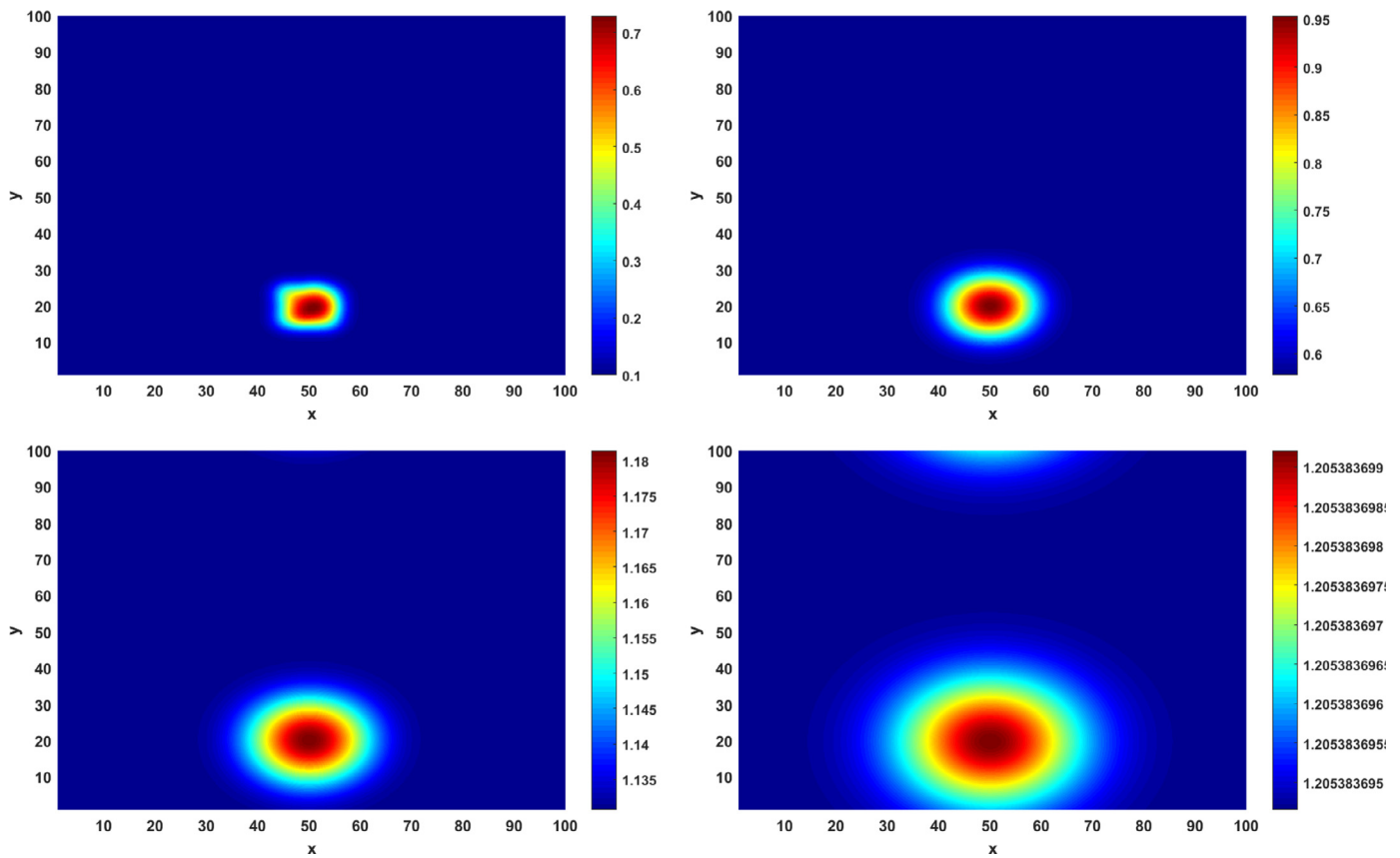
Fig. 1. Simulation of 2D phase-fields with a solid nucleus with $\sigma = 0.2$ for Example 1.

Table 1
The CPU time(s) for example 1.

Technique/number of collocation points	200	400	800	1600
MLPG2	35	91	171	451
MLPG5	145	281	419	789
MLPG6	175	341	615	918
DMLPG2 (Present method)	8	22	45	81
DMLPG5	24	51	103	252

where

$$\mathbf{a}_{k,:}^T(\mathbf{x}_i) = \vartheta_{k,i}(\mathbf{p}^T)\mathbf{M}^{-1}\mathbf{B}, \qquad k = 1, 2, 3, 4. \tag{31}$$

Finally, the above relations yield the algebraic system of equations

$$\mathbf{A}\mathbf{U}^n = \mathbf{b}. \tag{32}$$

4. Numerical simulations

In this section, in order to investigate the efficiency of the explained numerical model, several stochastic examples are given. To that end, the meshless method is applied for the space discretization where the Euler–Maruyama technique is used for the time discretization. In this paper, h and $\tau = T/N$ denote the mesh size and the step size of the time variable, respectively. We carried out the numerical computations using the **MATLAB 2017 b** program on an Intel Core i7 machine with 32 GB of memory. To check the convergence of the present numerical technique, we follow this strategy:

- Select a sufficiently small h^* and τ and obtain the numerical solution $U_{h^*}^\tau$ using these two parameters.
- Set $h^1, h^2, \ldots$ such that $h^* < h^i$ for $i = 1, 2, \ldots$ and obtain the corresponding numerical solutions $U_{h^1}^\tau, U_{h^2}^\tau, \ldots$ based on $h^1, h^2, \ldots$.
- Calculate

$$L_\infty^{h^*} = \max_{1 \leq j \leq M-1} \left| U_{h^*}^\tau(x_j) - U_{h^i}^\tau(x_j) \right|,$$

$$L_2^{h^*} = \left(\sum_{j=1}^{M-1} \left| U_{h^*}^\tau(x_j) - U_{h^i}^\tau(x_j) \right|^2 \right)^{\frac{1}{2}}$$

for $i = 1, 2, \ldots$. Note that the dimensions of $U_{h^*}^\tau$ and $U_{h^i}^\tau$ are different, but we only consider the common nodes in these solutions.

4.1. Example 1.

As the first example, we consider the growing nucleus with a noise term as follows

$$\tau\varepsilon\frac{\partial u}{\partial t} = 2\varepsilon\gamma\Delta u - \frac{18}{\varepsilon}\left(u^3 - 3u^2 + u\right) - 6mu(1-u) + \sigma\,\xi, \tag{33}$$
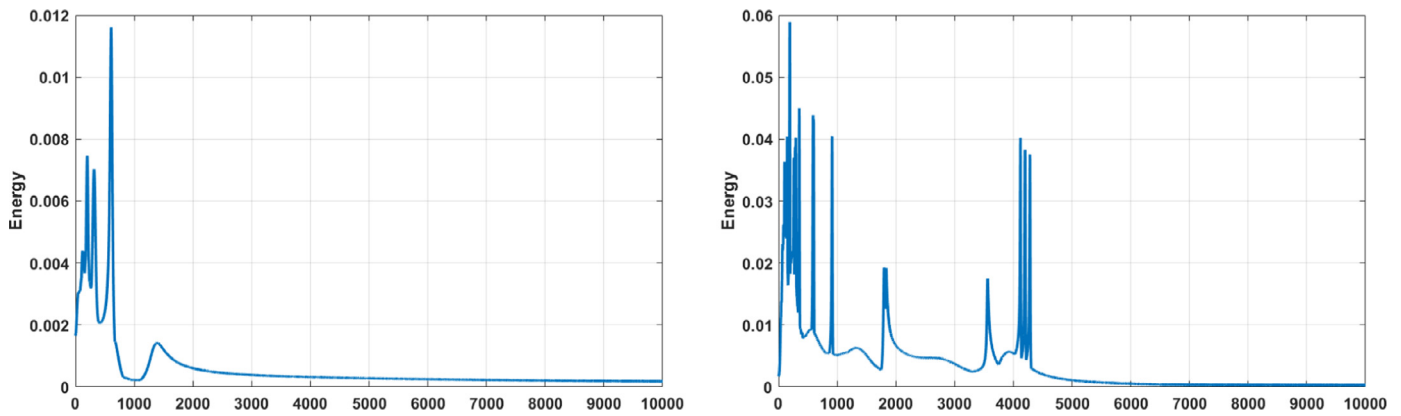
Fig. 2. Graph of energy with $\sigma = 0.05$ (left) and $\sigma = 0.2$ (right) for Example 2. The higher white noise effect gives rise to higher energy variation.

Table 2

A comparison between the LMK, LRBFs from Dehghan and Abbaszadeh [11] and the present method with $h^* = 1/1024$ based on the reference solution and $L_\infty^{h^*}$ error for Test problem 1.

h	1/8	1/16	1/32	1/64
LMK	2.8702×10^{-1}	1.0148×10^{-1}	7.0105×10^{-2}	3.5431×10^{-2}
LRBFs	1.0056×10^{-1}	7.5338×10^{-2}	4.9870×10^{-2}	2.4908×10^{-2}
MLS-RBFs	2.0112×10^{-1}	8.8125×10^{-2}	3.6492×10^{-2}	1.0104×10^{-2}
MK-RBFs	1.5101×10^{-1}	7.4880×10^{-2}	2.9908×10^{-2}	9.0141×10^{-3}
Present method	9.8760×10^{-2}	2.7746×10^{-2}	1.0020×10^{-2}	8.3072×10^{-3}

Table 3

A comparison between LMK, LRBFs from Dehghan and Abbaszadeh [11] and the present method with $h^* = 1/1024$ based on the reference solution for test problem 2.

h	Present method $L_2^{h^*}$	$L_\infty^{h^*}$	LRBF-MK [11] $L_2^{h^*}$	$L_\infty^{h^*}$
1/4	3.0321×10^{-2}	1.0326×10^{-2}	3.5514×10^{-2}	1.9561×10^{-2}
1/8	8.3014×10^{-2}	5.3015×10^{-3}	1.9879×10^{-2}	8.6641×10^{-3}
1/16	4.2036×10^{-3}	1.9890×10^{-3}	9.0501×10^{-3}	4.2670×10^{-3}
1/32	2.8423×10^{-3}	1.0012×10^{-3}	4.1431×10^{-3}	1.9879×10^{-3}
1/64	6.3742×10^{-4}	3.1180×10^{-4}	2.7031×10^{-3}	9.0243×10^{-4}

with the periodic boundary conditions. The initial condition can be found in [11] and $m = 0.25$. Then, we give a brief information of the explained model that is taken from Janssens et al. [45].

Let us consider a system with constant temperature [45] thus the Ginzburg–Landau entropy functional is [45]

$$\mathcal{E}(u) = \int_\Omega \left(F(u) - \varepsilon a(\nabla u) + \frac{1}{\varepsilon} W(u) \right) dx, \tag{34}$$

as for a two-phase system

$$a(\nabla u) = \gamma |\nabla u|^2, \tag{35}$$

where γ can be found in [45]. In case of the potential entropy density, we have

$$W(u) = \gamma u^2 (1 - u)^2. \tag{36}$$

Applying the variational derivative of the entropy functional, we will get

$$\tau \varepsilon \frac{\partial u}{\partial t} = \frac{\delta E(u)}{\delta u} = \frac{\partial E}{\partial u} - \nabla \cdot \frac{\partial E}{\partial (\nabla u)}. \tag{37}$$

Afterwards, we can conclude that the equation has the form

$$\tau \varepsilon \frac{\partial u}{\partial t} = 2\varepsilon \gamma \Delta u - \frac{18}{\varepsilon} \left(u^3 - 3u^2 + u \right) - 6mu(1 - u). \tag{38}$$

Eq. (38) is used to model crystal growth from an undercooled pure substance [45]. Then the stochastic equation can be derived by adding the noise term.

Fig. 1 illustrates the approximation of the 2D simulation of phase-field with a solid nucleus at the bottom of the computational domain for $T = 1$ (top left), $T = 2$ (top right), $T = 4$ (bottom left) and $T = 6$ (bottom right) with $\varepsilon = 0.01$, $\tau = 0.001$, $\sigma = 0.2$ (the noise measure) and the periodic boundary condition for Example 1.

Table 1 compares the CPU time for the MLPG2, MLPG 5, MLPG6, DMLPG2, and DMLPG5 methods. The CPU time for DMLPG2, i.e., the present method is lower than the other meshless techniques. Table 2 presents a comparison between LMK, LRBFs from Dehghan and Abbaszadeh [11] and the present method with $h^* = 1/1024$ based on the reference solution and the $L_\infty^{h^*}$ error for test problem 1.

4.2. Example 2.

The stochastic Cahn–Hilliard–Cook equation can be defined as [32]

$$\frac{\partial u}{\partial t} = M \nabla^2 \left(u^3 - \frac{3}{2} u^2 + \frac{1}{2} u - \varepsilon^2 \nabla^2 u \right) + \sigma \xi \tag{39}$$
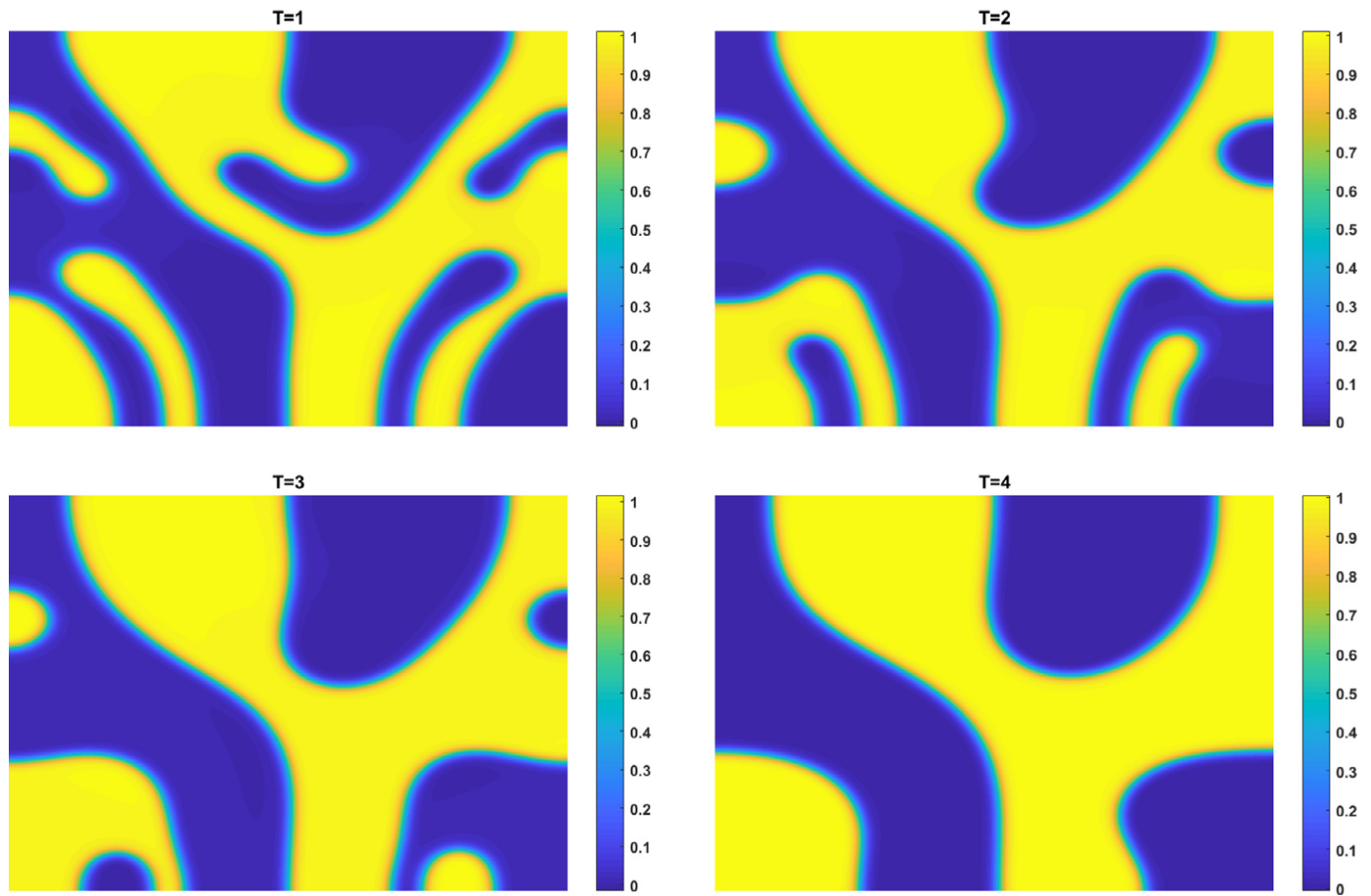
Fig. 3. Approximation of the solution with $\sigma = 0.2$ and $\epsilon = 4h \arctan(0.9)$ for Example 2 during different times.

with the boundary conditions

$$\nabla u \cdot \mathbf{n} = 0, \qquad \nabla \left(u^3 - \frac{3}{2}u^2 + \frac{1}{2}u - \epsilon^2 \nabla^2 u \right) \cdot \mathbf{n} = 0. \tag{40}$$

Here, in this example, we use the initial condition

$$u(x, y, 0) = 0.5 + 0.17 \cos(\pi x) \cos(2\pi y) + 0.2 \cos(3\pi x) \cos(\pi y). \tag{41}$$

Since Eq. (39) is a fourth-order equation, we apply a new variable for converting Eq. (39) to a system of two second-order PDEs. By adding the white noise to the system, we have

$$\begin{cases} \dfrac{\partial u}{\partial t} = M\nabla^2 w + \sigma\, \xi, \\[2mm] w = u^3 - \dfrac{3}{2}u^2 + \dfrac{1}{2}u - \epsilon^2 \nabla^2 u, \end{cases}$$

with the boundary conditions

$$\nabla u \cdot \mathbf{n} = 0, \quad \nabla w \cdot \mathbf{n} = 0,$$

and the initial conditions

$$u(x, y, 0) = 0.5 + 0.17 \cos(\pi x) \cos(2\pi y) + 0.2 \cos(3\pi x) \cos(\pi y),$$
$$w(x, y, 0) = u(x, y, 0)^3 - \frac{3}{2}[u(x, y, 0)]^2 + \frac{1}{2}u(x, y, 0) - \epsilon^2 \nabla^2 u(x, y, 0).$$

Furthermore, we assume that $V(u, T)$ is a potential energy landscape which can be approximated as follows [46]

$$V(u, T) = c_1(T)u^2 + c_2(T)u^4, \tag{42}$$

such that the coefficients c_1 and c_2 are connected to the precise Hamiltonian of the system [46]. We rewrite the potential as

$$V = \frac{1}{4}\left(a - (bu)^2 \right)^2. \tag{43}$$

Now in order to achieve the energy functional, we combine the potential [46]

$$\mathcal{F}[u(x, t)] = \int_{\Omega} \left(\frac{1}{4}\left(a - (bu)^2 \right)^2 + \frac{\gamma}{2}|\nabla u|^2 \right) dx, \tag{44}$$

where the constant γ penalizes the phase boundaries.

The stochastic equation allows us to model the thermal fluctuation. Now we apply the RBF technique to obtain the solution of Cahn–Hilliard–Cook equation. For the time discretization, we used the semi-implicit Euler–Maruyama technique to solve the equation on $[0, T]$. Fig. 2 shows the graph of energy with $\sigma = 0.05$ (left figure) and $\sigma = 0.2$ (right figure) for Example 2. From Fig. 2, we can conclude that the energy for different values of σ, after a specified time, is stable. Fig. 3 presents the approximated solution with $\sigma = 0.2$ and $\epsilon = 4h \arctan(0.9)$ using the present method based on the several values of final time for Example 2. Furthermore, Fig. 4 illustrates the graphs of approximation solution with $\sigma = 0.2$ and $\epsilon = 0.01$ applying the introduced technique for Example 2. From Figs. 3 and 4, we can see that the solution of this model is stable by increasing the final time. The effect of the white noise is pronounced in Fig. 4.

Table 3 shows a comparison between LMK and LRBFs from Dehghan and Abbaszadeh [11] and present methods with $h^* = 1/1024$ based on the reference solution for test problem 2.
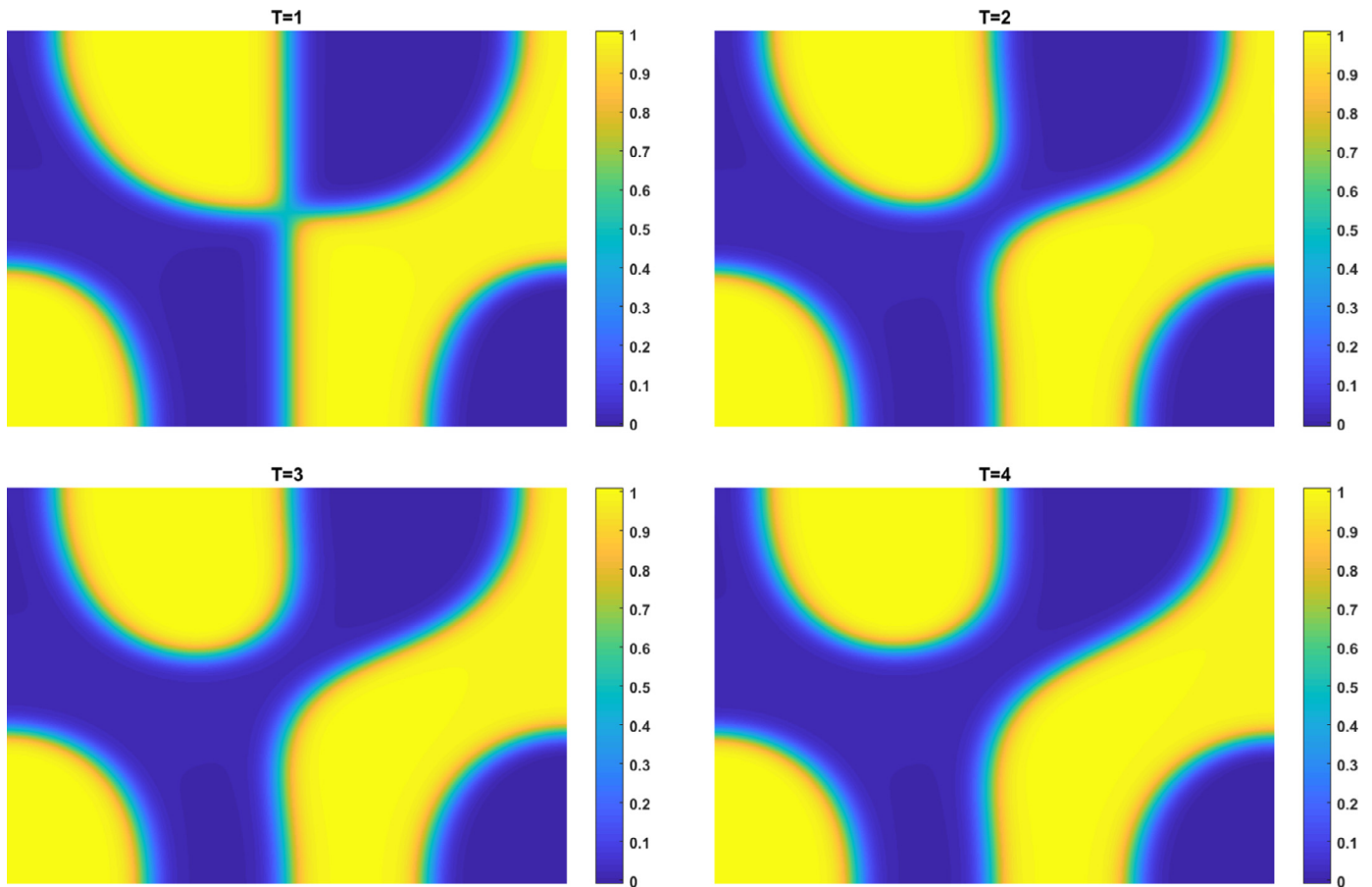
Fig. 4. Approximated solution with $\sigma = 0.2$ and $\epsilon = 0.01$ for Example 2 during different times.

4.3. Example 3.

The stochastic Swift–Hohenberg equation can be written as

$$\frac{\partial u}{\partial t} = -\mu(u) - Dk^4u - \Delta(2Dk^2u + D\Delta u) + \sigma\xi \qquad \text{in } \Omega \times (0, T), \qquad (45)$$

$$\nabla(2Dk^2u + D\Delta u) \cdot \mathbf{n} = 0 \qquad \qquad \text{on } \Gamma \times [0, T], \qquad (46)$$

$$\nabla u \cdot \mathbf{n} = 0 \qquad \qquad \text{on } \Gamma \times [0, T], \qquad (47)$$

$$u(x, 0) = u_0(x) \qquad \qquad \text{in } \overline{\Omega}. \qquad (48)$$

Let $\Omega \subset \mathbb{R}^2$ be the computational geometry, the free-energy functional is considered as [34]

$$\mathcal{E}(u) = \int_\Omega \left(\Psi(u) + \frac{D}{2}\left[(\Delta u)^2 - 2k^2|\nabla u|^2 + k^4u^2 \right] \right) dx. \qquad (49)$$

Here D and k are constant and

$$\Psi(u) = -\frac{\epsilon}{2}u^2 - \frac{g}{3}u^3 + \frac{1}{4}u^4, \qquad (50)$$

where $\epsilon, g \in \mathbb{R}^+$. The Swift–Hohenberg equation is [34]

$$\frac{\partial u}{\partial t} = -\frac{\delta\mathcal{E}}{\delta u} = \Psi'(u) + Dk^4u + 2Dk^2\Delta u + D\Delta^2 u. \qquad (51)$$

For this case, the initial condition is [34]

$$u(x, y, 0) = \begin{cases} 1 & x_1 < x < x_2, \\ 0 & x_2 < x, \\ 0 & x < x_1, \end{cases}$$

where

$$x_1 = \sin\left(\frac{2\pi}{10}y\right) + 15, \qquad x_2 = \cos\left(\frac{2\pi}{10}y\right) + 25. \qquad (52)$$

At first, we consider

$$w = 2Dk^2u + D\Delta u. \qquad (53)$$

Afterwards, the new problem with the white noise is

$$f(x) = \begin{cases} \dfrac{\partial u}{\partial t} = -\mu(u) - Dk^4u - \Delta\left(2Dk^2u + D\Delta u\right) + \sigma\xi & \text{in } \Omega \times (0, T) \\ w = 2Dk^2u + D\Delta u & \text{in } \Omega \times (0, T). \end{cases}$$

with the boundary conditions

$$\nabla u \cdot \mathbf{n} = 0, \quad \nabla w \cdot \mathbf{n} = 0 \quad \text{on } \Gamma \times [0, T]. \qquad (54)$$

Fig. 5 shows the evolution of the approximated solution on [0, 40] × [0, 40] with $\sigma = 0.2$ for Example 3 where the solution is obtained using the introduced meshless technique. Again, the effect of the white noise is tangible.
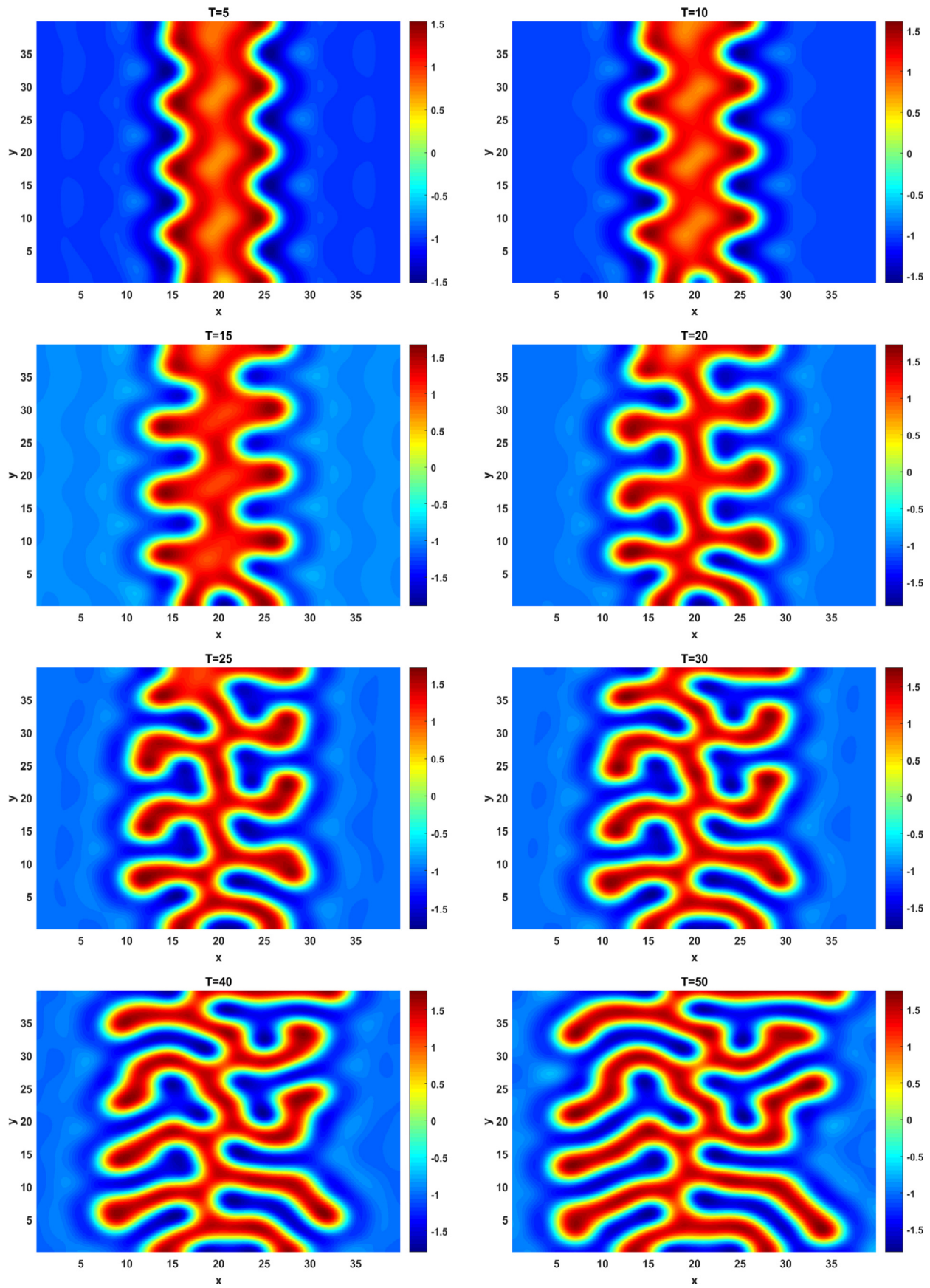
Fig. 5. Approximated solution on $\Omega = [0, 40] \times [0, 40]$ with $\sigma = 0.2$ for Example 3 for different times.
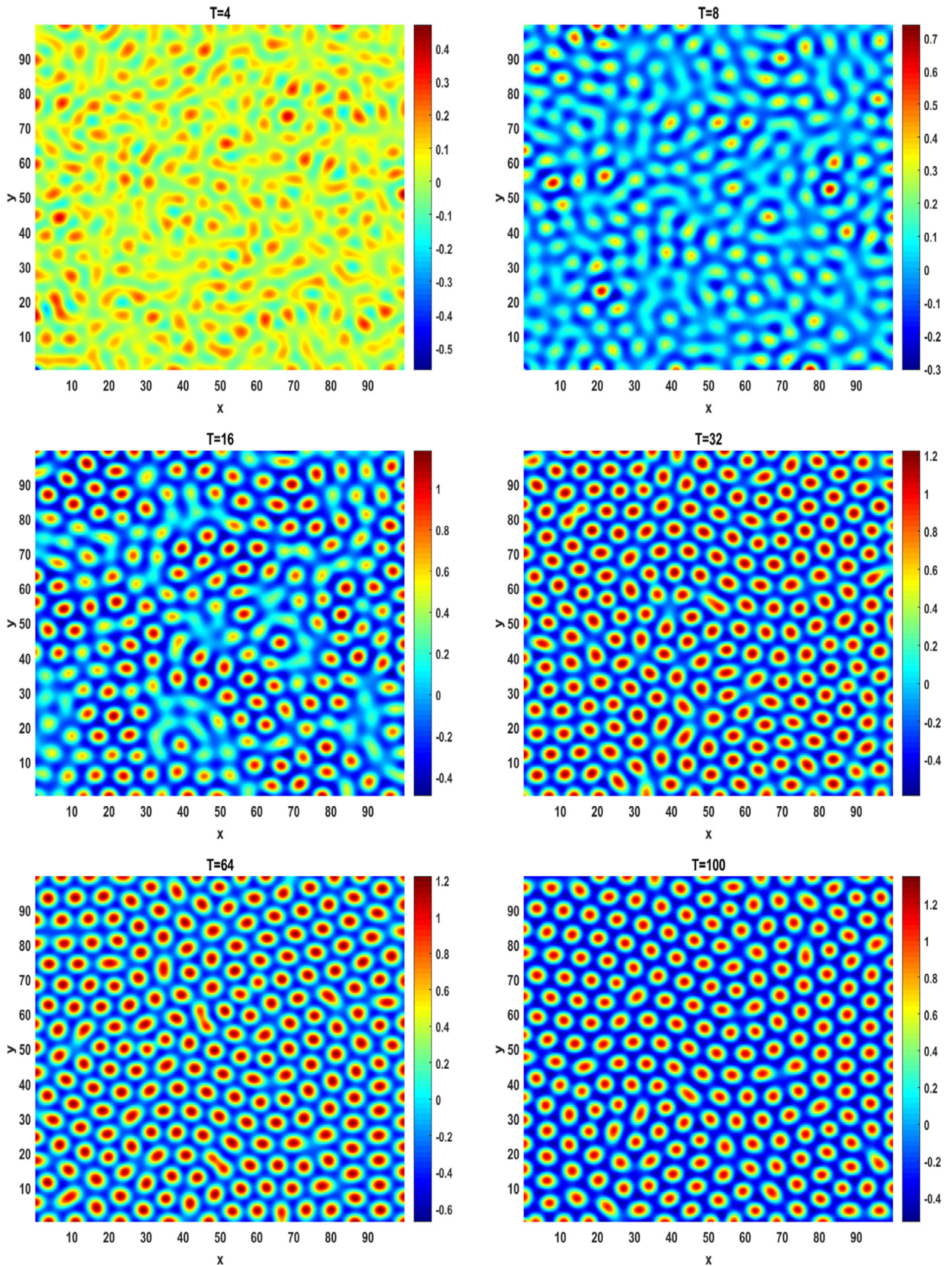
Fig. 6. Approximated solution on $\Omega = [0, 100] \times [0, 100]$ with $\sigma = 0.2$ for Example 4 during different time intervals.
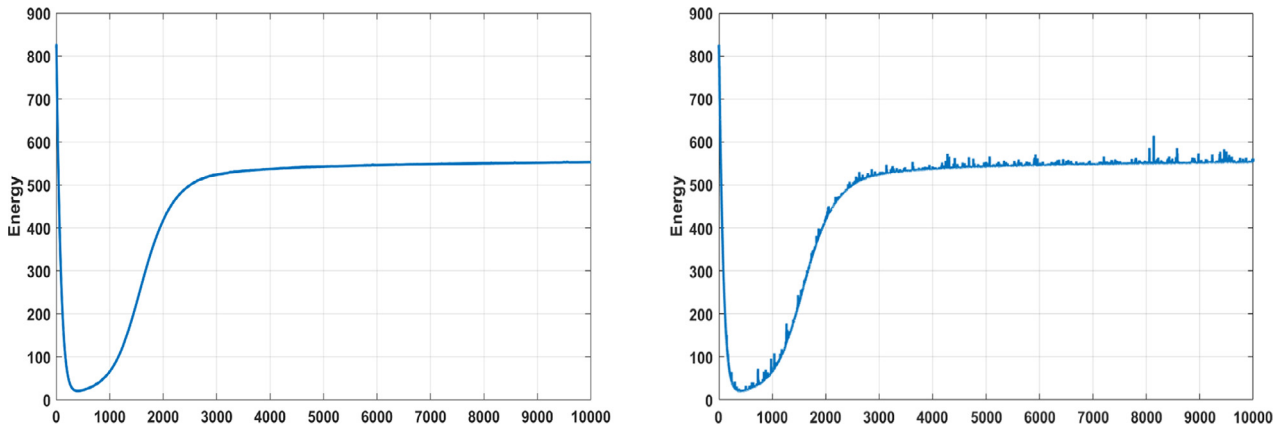
Fig. 7. Graph of energy with $\sigma = 0.05$ (left) and $\sigma = 0.2$ (right) for Example 4. The higher noise increases the energy fluctuations.
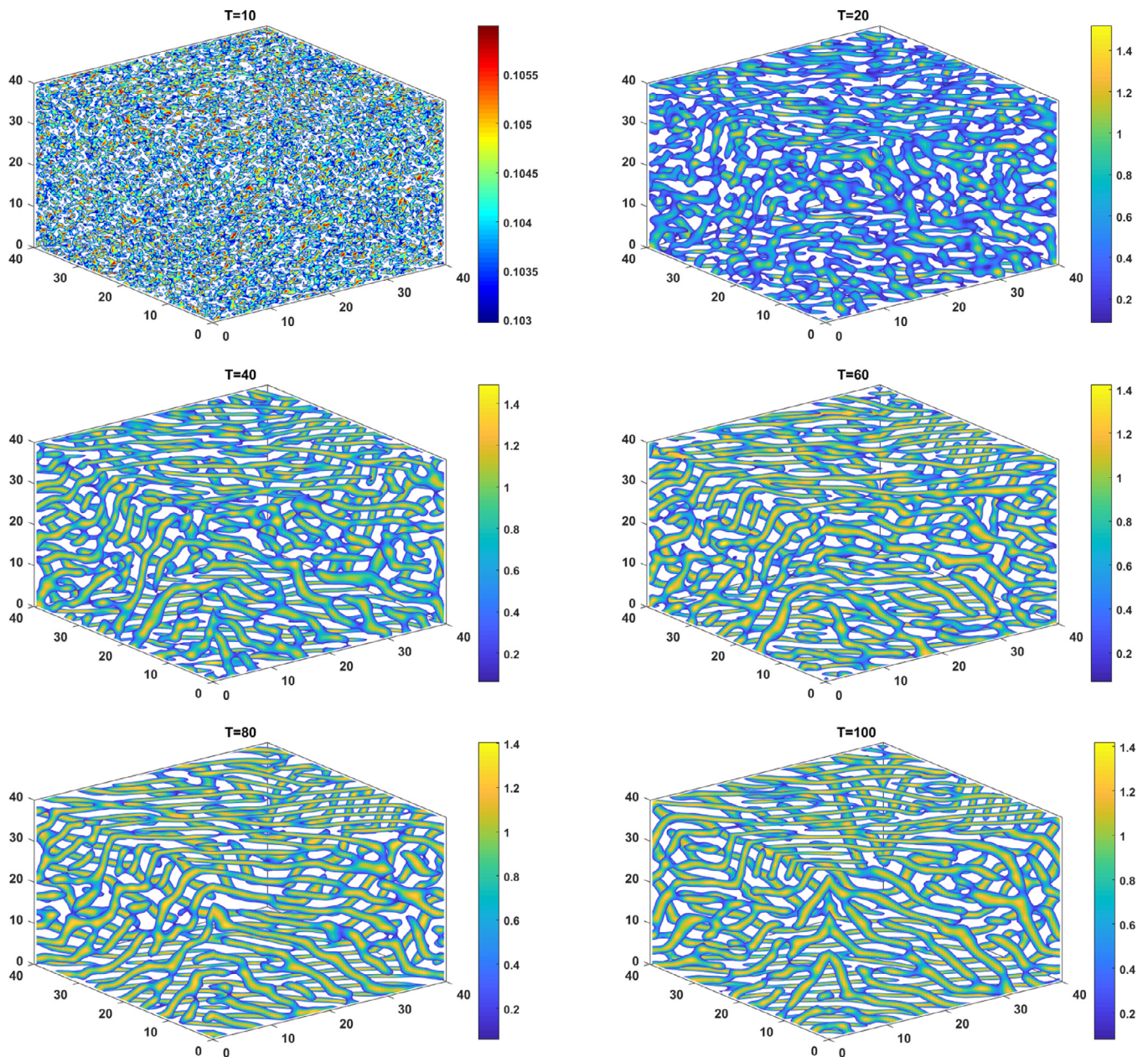

Fig. 8. Time evolution of the approximation solution of (56) on domain $[0,40] \times [0,40] \times [0,40]$ using the presented meshless method for Example 5.

4.4. Example 4.

As the next stochastic model, we use the stochastic Swift–Hohenberg equation [47]

$$\frac{\partial u}{\partial t} = \varepsilon u - (\Delta + 1)^2 u + g u^2 - u^3 + \sigma \xi \quad \text{in } \Omega \times (0, T). \tag{55}$$

Here, we added white noise to the problem and the periodic boundary conditions as well as random initial condition are used.

The approximated solution on $\Omega = [0, 100] \times [0, 100]$ with $\sigma = 0.2$ has been depicted in Fig. 6 for Example 4 during different time intervals. The figure demonstrates the hexagonal instability dynamics as well. Also, Fig. 7 displays the graph of energy with $\sigma = 0.05$ (left) and $\sigma = 0.2$ (right) for the aforementioned example.

4.5. Example 5.

The 3D stochastic Cahn–Hilliard–Cook equation can be considered as [7]

$$\begin{cases} \dfrac{\partial u}{\partial t} = M \nabla^2 w + \sigma \xi & \text{in } \Omega \times (0, T), \\ w = u^3 - u - \varepsilon^2 \nabla^2 u & \text{in } \Omega \times (0, T) \end{cases} \tag{56}$$

with no-flux boundary conditions and the following initial conditions

$$\begin{cases} u(x, y, z, 0) = -0.003 + 0.006 \, \omega, \\ w(x, y, z, 0) = u^3(x, y, z, 0) - u(x, y, z, 0) - \varepsilon^2 \nabla^2 u(x, y, z, 0). \end{cases} \tag{57}$$

We should note that in the initial condition, ω is an array of random numbers uniformly distributed between 0 and 1. Fig. 8 illustrates the approximation solution of Eq. (56) with $\sigma = 0.1$, $\tau = 10^{-4}$ and 4000 collocation points on domain $[0, 40] \times [0, 40] \times [0, 40]$ by applying the introduced numerical technique for Example 5 for different time intervals from $T = 10$ to $T = 100$.

5. Conclusions

The meshless techniques based on the collocation method are one of the most efficient numerical approaches to solve stochastic PDEs. The direct MLPG (DMLPG) technique is an extension of the MLPG method to reduce the CPU time. In the current investigation, the authors employed the DMLPG 2 method, i.e., the direct local meshless technique in order to solve the stochastic Cahn–Hilliard–Cook as well as stochastic Swift–Hohenberg equations. First, to achieve the semi-discrete scheme the Euler–Maruyama method applied to discretize the time variable. Afterwards, the DMLG 2 technique is used to obtain a full-discrete scheme. The proposed numerical technique is applied to the two- and three-dimensional Cahn–Hilliard–Cook and stochastic Swift–Hohenberg equations. Also, we studied the effect of the noise parameter in the approximation solution and the energy graph. Finally, some numerical examples have been presented to validate the efficiency of the proposed numerical technique. The results clarify the computational capability of the developed method for the stochastic time-dependent problems.

Acknowledgments

References

[1] Cahn JW, Hilliard JE. Free energy of a nonuniform system. I. Interfacial free energy. J Chem Phys 1958;28(2):258–67.

[2] Cogswell DA. A phase-field study of ternary multiphase microstructures. Massachusetts Institute of Technology; 2010. Ph.D. thesis.

[3] Khain E, Sander LM. Generalized Cahn–Hilliard equation for biological applications. Phys Rev E 2008;77(5):051129.

[4] Miranville A. The Cahn–Hilliard equation and some of its variants. AIMS Math 2017;2(3):479–544.

[5] Chossat P, Faye G. Pattern formation for the Swift–Hohenberg equation on the hyperbolic plane. J Dyn Differ Equ 2015;27(3–4):485–531.

[6] Morgan D, Dawes JH. The Swift–Hohenberg equation with a nonlocal nonlinearity. Phys D Nonlinear Phenom 2014;270:60–80.

[7] Du Q, Ju L, Tian L. Finite element approximation of the Cahn–Hilliard equation on surfaces. Comput Methods Appl Mech Eng 2011;200(29–32):2458–70.

[8] Gómez H, Calo VM, Bazilevs Y, Hughes TJ. Isogeometric analysis of the Cahn–Hilliard phase-field model. Comput Methods Appl Mech Eng 2008;197(49–50):4333–52.

[9] Fernandino M, Dorao C. The least squares spectral element method for the Cahn–Hilliard equation. Appl Math Model 2011;35(2):797–806.

[10] Dehghan M, Mohammadi V. The numerical solution of Cahn–Hilliard (CH) equation in one, two and three-dimensions via globally radial basis functions (GRBFs) and RBFs-differential quadrature (RBFs-DQ) methods. Eng Anal Bound Elem 2015;51:74–100.

[11] Dehghan M, Abbaszadeh M. The meshless local collocation method for solving multi-dimensional Cahn-Hilliard, Swift–Hohenberg and phase field crystal equations. Eng Anal Bound Elem 2017;78:49–64.

[12] Pérez-Moreno SS, Chavarría SR, Chavarría GR. Numerical solution of the Swift–Hohenberg equation. In: Experimental and computational fluid mechanics. Springer; 2014. p. 409–16.

[13] Lloyd DJ, Sandstede B, Avitabile D, Champneys AR. Localized hexagon patterns of the planar Swift–Hohenberg equation. SIAM J Appl Dyn Syst 2008;7(3):1049–100.

[14] Atluri SN, Zhu T. A new meshless local Petrov–Galerkin (MLPG) approach in computational mechanics. Comput Mech 1998;22(2):117–27.

[15] Mirzaei D, Schaback R, Dehghan M. On generalized moving least squares and diffuse derivatives. IMA J Numer Anal 2012;32(3):983–1000.

[16] Mirzaei D, Schaback R. Direct meshless local Petrov–Galerkin (DMLPG) method: a generalized MLS approximation. Appl Numer Math 2013;68:73–82.

[17] Mirzaei D, Schaback R. Solving heat conduction problems by the direct meshless local Petrov–Galerkin (DMLPG) method. Numer Algorithms 2014;65(2):275–91.

[18] Ramezani M, Mojtabaei M, Mirzaei D. DMLPG solution of the fractional advection–diffusion problem. Eng Anal Bound Elem 2015;59:36–42.

[19] Taleei A, Dehghan M. Direct meshless local Petrov–Galerkin method for elliptic interface problems with applications in electrostatic and elastostatic. Comput Methods Appl Mech Eng 2014;278:479–98.

[20] Mazzia A, Pini G, Sartoretto F. Numerical investigation on direct MLPG for 2D and 3D potential problems. Comput Model Eng Sci(CMES) 2012;88(3):183–209.

[21] Sartoretto F, Mazzia A, Pini G. The DMLPG meshless technique for Poisson problems. Appl Math Sci 2014;8(164):8233–50.

[22] Shivanian E. On the convergence analysis, stability, and implementation of meshless local radial point interpolation on a class of three-dimensional wave equations. Int J Numer Methods Eng 2016;105(2):83–110.

[23] Atluri S, Zhu T. New concepts in meshless methods. Int J Numer Methods Eng 2000;47(1–3):537–56.

[24] Wang J, Liu G. A point interpolation meshless method based on radial basis functions. Int J Numer Methods Eng 2002;54(11):1623–48.

[25] Mirzaei D. A greedy meshless local Petrov–Galerkin methodbased on radial basis functions. Numer Methods Part Differ Equ 2016;32(3):847–61.

[26] Cahn JW. On spinodal decomposition. Acta Metall 1961;9(9):795–801.

[27] Zaeem MA, El Kadiri H, Wang PT, Horstemeyer MF. Investigating the effects of grain boundary energy anisotropy and second-phase particles on grain growth using a phase-field model. Comput Mater Sci 2011;50(8):2488–92.

[28] Wise SM, Lowengrub JS, Frieboes HB, Cristini V. Three-dimensional multi-species nonlinear tumor growth–I: model and numerical method. J Theor Biol 2008;253(3):524–43.

[29] Mamivand M, Zaeem MA, El Kadiri H. A review on phase field modeling of martensitic phase transformation. Comput Mater Sci 2013;77:304–11.

[30] Zhou C, Kumar S. Two-dimensional two-layer channel flow near a step. Chem Eng Sci 2012;81:38–45.

[31] Blomker D, Sander E, Wanner T. Degenerate nucleation in the Cahn–Hilliard–Cook model. SIAM J Appl Dyn Syst 2016;15(1):459–94.

[32] Khodadadian A, Parvizi M, Abbaszadeh M, Dehghan M, Heitzinger C. A multilevel Monte Carlo finite element method for the Cahn–Hilliard–Cook equation. 2018; submitted for publication.

[33] Swift J, Hohenberg PC. Hydrodynamic fluctuations at the convective instability. Phys Rev A 1977;15(1):319.

[34] Gomez H, Nogueira X. A new space–time discretization for the Swift–Hohenberg equation that strictly respects the Lyapunov functional. Commun Nonlinear Sci Numer Simul 2012;17(12):4930–46.

[35] Akyildiz FT, Siginer DA, Vajravelu K, Van Gorder RA. Analytical and numerical results for the Swift–Hohenberg equation. Appl Math Comput 2010;216(1):221–6.

[36] Zhao X, Liu B, Zhang P, Zhang W, Liu F. Fourier spectral method for the modified Swift–Hohenberg equation. Adv Differ Equ 2013;2013(1):156.

[37] Kudryashov NA, Sinelshchikov DI. Exact solutions of the Swift–Hohenberg equation with dispersion. Commun Nonlinear Sci Numer Simul 2012;17(1):26–34.

[38] McCalla S, Sandstede B. Snaking of radial solutions of the multi-dimensional Swift–Hohenberg equation: a numerical study. Phys D Nonlinear Phenom 2010;239(16):1581–92.

[39] Park SH, Park JY. Pullback attractor for a non-autonomous modified Swift–Hohenberg equation. Comput Math Appl 2014;67(3):542–8.

[40] Gabbrielli R. Foam geometry and structural design of porous material. University of Bath; 2009. Ph.D. thesis.

[41] Lega J, Moloney J, Newell A. Swift–Hohenberg equation for lasers. Phys Rev Lett 1994;73(22):2978.

[42] Peletier LA, Rottschäfer V. Pattern selection of solutions of the Swift–Hohenberg equation. Phys D Nonlinear Phenom 2004;194(1–2):95–126.

[43] Bodenschatz E, Pesch W, Ahlers G. Recent developments in Rayleigh–Bénard convection. Annu. Rev Fluid Mech 2000;32(1):709–78.

[44] Gao P. The stochastic Swift–Hohenberg equation. Nonlinearity 2017;30(9):3516.

[45] Janssens KGF, Raabe D, Kozeschnik E, Miodownik MA, Nestler B. Computational materials engineering: an introduction to microstructure evolution. Academic Press; 2010.

[46] Ursell T.S. Cahn–Hilliard kinetics and spinodal decomposition in a diffuse system, California Institute of Technology, Pasadena, CA 91125, October 2009.

[47] Klapp J, Medina A. Experimental and computational fluid mechanics. Springer; 2013.